Journal of Basic and Applied Engineering Research
Print ISSN: 2350-0077; Online ISSN: 2350-0255; Volume 2, Number 15; April-June, 2015 pp. 1266-1271

http://www.krishisanskriti.org/jbaer.html

Compositional Dependence of Structural and Dielectric Properties of Lead FreeBa($Zr_{0.2}Ti_{0.8}$) O_3-x($Ba_{0.7}Ca_{0.3}$)TiO_3Electroceramics

Chandan Bhardwaj[1] and Davinder Kaur[2]

[1]*Department of Physics, NSCBM Govt. Degree College, Hamirpur (HP)- 177001, India*
[2]*Department of Physics and Centre of Nanotechnology, Indian Institute of Technology Roorkee, Roorkee 247667, India*

Abstract—*A comparative study of structural and electric properties of lead free electroceramics, $Ba(Zr_{0.2}Ti_{0.8})O_3 - x(Ba_{0.7}Ca_{0.3})TiO_3$ or BZT-xBCT (with x being the molar fraction of BCT), prepared by solid state reaction technique, was conducted in the entire range from x=0 to x=1. The XRD and FESEM analysis established the structural transition and different phases as function of Zr/Ti and Ba/Ca ratios. All the effects and trends observed in ceramics were found to be due to the interplay of two competing compositions i.e. decreasing Zr and increasing Ca with increasing x. The phase transitions from rhombohedral to tetragonal phase were identified in the composition range of $0 \leq x \leq 1$.The dielectric studies revealed that Morphotrophic Phase Boundary (MPB) composition at x=0.5 (50BCT) exhibits the highest dielectric constant and lowest loss among all the compositions. The grain size effect and its influence on dielectric and properties were discussed in detail.*

Keywords*: A. Electroceramics; C. XRD; C. Scanning Electron Microscopy; D. Dielectric.*

1. INTRODUCTION

The substantial efforts have been dedicated to the development of the new lead free material worldwide as there is an urgent need to develop a non-Pb substitute that can compete with PZT. The main aim of the present study is to investigate the structural and dielectric behaviour of lead free BZT-*x* BCTceramic that shows anomalously high dielectric constant at x=0.5 [1]. The barium titanate ($BaTiO_3$) and isovalent substituted $BaTiO_3$ are the promising candidates for potential use in the applications of capacitors, microwave communications and optoelectronic devices. In the present study, we made a solid solution of BZT and BCT (BZT-*x*BCT) where Ba and Ca ions occupy the *A* sites of the ABO_3 perovskite structure with the ionic radius of Ca^{2+} (0.99 Å) being smaller than that of Ba^{2+} (1.35 Å) and Zr and Ti ions occupy the *B* sites with the ionic radius of Zr^{4+} (0.98 Å) being larger than that of Ti^{4+} (0.72 Å) [2, 3]. We found that decreasing Zr and increasing Ca contents govern the behavioral trends from *x*=0 to *x*=0.5 and *x*=0.5 to *x*=1, respectively. The grain size effect could explain the extraordinary characteristics shown by optimized composition at *x*=0.5.

2. EXPERIMENTAL

BZT-*x*BCT ceramics with composition *x*=0, *x*=0.1, *x*=0.2, *x*=0.3, *x*=0.4, *x*=0.5, *x*=0.6, *x*=0.7, *x*=0.8, *x*=0.9 and *x*=1; hereafter abbreviated as BZT, 10BCT, 20BCT, 30BCT, 40BCT, 50BCT, 60BCT, 70BCT, 80BCT, 90BCT and BCT, respectively, were prepared by conventional solid state reaction method. High purity starting oxide powders of $BaCO_3$ (99.0%), $CaCO_3$ (99.0%), ZrO_2 (99.0%) and TiO_2(99.5%)were thoroughly mixed with addition of alcohol, ground, dried and then calcined at 1200^o Cfor 6 hours. After calcinations, the powder was again ground and compacted in the form of pallets with 1mm of thickness and 5mm of diameter, isostatically pressed at 10 tons. Finally, the pallets were sintered at 1450^o C for 5 hours in the presence of air and then cooled to room temperature. The orientation and crystalline of the ceramics were studied using Bruker D8 Advanced Diffract meter of Cu Kα (1.54Å) radiations in θ - 2θ) geometry. The surface topography and microstructures were analyzed using field emission scanning electron microscopy FESEM (FEI Quanta 200 F). The frequency dependence of the dielectric properties was measured by Agilent 4294A impedance analyzer in the frequency range of 1kHz to 2MHz.

3. RESULTS AND DISCUSSION

Fig. 1shows the room temperature XRD plots of BZT-*x*BCT ceramics and corresponding values of various parameters are mentioned in **Table 1**.It can be seen that all the samples show pure perovskite structure, suggesting that Ca and Zr diffuse in to the BaTiO3 lattice to form a stable solid solution (**Figure1(a)**). At room temperature, the ceramic undergoes a transformation from rhombohedral at x=0 to tetragonal phase at x=1, featured with gradual increase in splitting of (002)/(200) peaks at around 2θ=45° as shown in **Figure1(c)**[4]. This transformation is further verified by

gradually increasing tetragonal distortion [(c/a-1)×100] with increasing *x* as given in **Table 1**. Therefore, it can be suggested that rhombohedral and tetragonal phase coexist in the vicinity of MPB composition at *x*=0.5 [1].

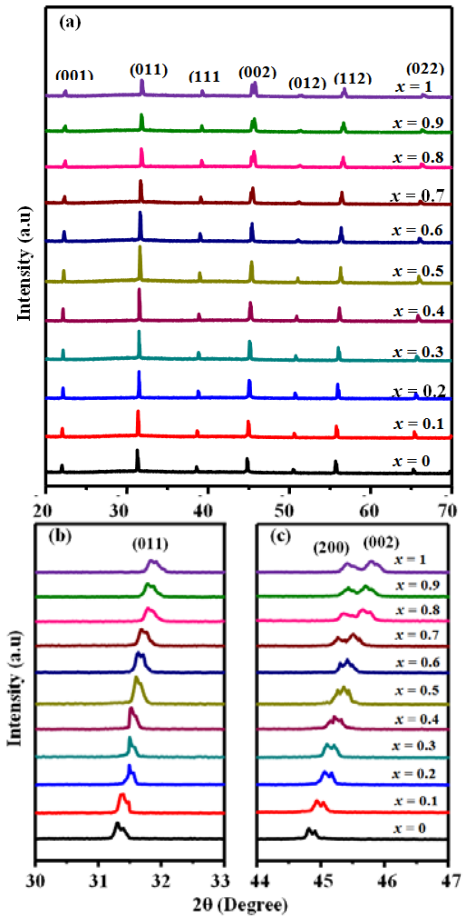

Fig. 1: XRD pattern of BZT-*x*BCT ceramic, (a)*x* = 0 to *x* = 1, (b) Normalized diffractograms of maximum intensity peak (011) and (c) (002)/(200) peak splitting at 2θ = 45^0.

In order to obtain the true value of the lattice constant we made use of an extrapolation technique by plotting the calculated lattice constants against a function *f(θ)* defined as [5, 6]:

$$f(\theta) = \frac{1}{2}\left(\frac{\cos^2\theta}{\sin\theta} + \frac{\cos^2\theta}{\theta}\right)$$

where θ is the Bragg's angle. **Fig. 2** shows the *a* versus *f(θ)* plots for the lattice parameters calculated from the peak position of each diffraction plane for each sample. Extrapolation of the plots to *x* = 0 yields the true lattice parameter. Thus, the true lattice parameter may be taken as the average value for all the reflecting planes in the X-ray spectrum. It can be observed from **Fig. 2** that the points do not lie on a straight line as would be expected of an unstrained perfect polycrystalline material. The values of lattice parameter given in **Table 1**, ascertain the shrinkage of lattice with increasing x and development of compressive strain in the materials.

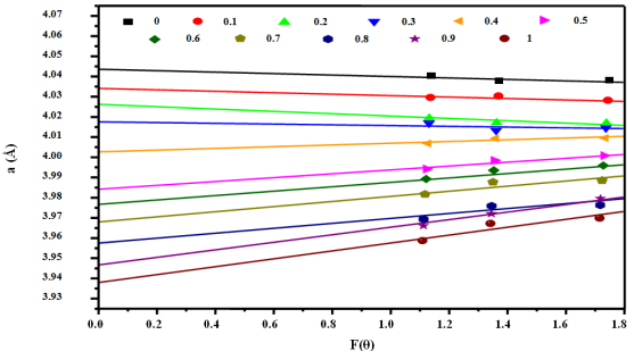

Fig. 2: Nelson-Riley Plot to calculate Lattice Parameter.

Fig. 1(b) shows the intensity and shifting of maximum intensity peak (110). The diffraction peaks were found to be shifted to higher angles as we moved from x=0 to x=1. The substitution of Ti^{4+} by Zr^{4+} expands the lattice of ceramics as ionic radii of Zr^{4+} are larger than that of Ti^{4+}. Hence shrinking lattice with decreasing Zr contents, causes shifting of diffraction peaks to higher angles [2, 7, 8]. The effect of increasing Ca contents with increasing *x* adds on to this shifting to higher angles as lattice constant further shrinks with the increase in Ca^{2+} ions at the Ba^{2+} sites, due to smaller ionic radii of Ca^{2+} over Ba^{2+}[9, 10]. It is also evident that the x-ray peak intensity increases gradually form x=0 to x= 0.5 and then, decreases from x=0.5 to x=1. This is indicative of degree of crystallinity and average crystallite size.

The average crystallite size (*D*)and strain (ε) in the sample were determined using the Williamson-Hall Equation [11-12]:

$$\beta_{hkl} = \frac{K\lambda}{D\cos\theta} + 4\varepsilon\tan\theta \quad \Rightarrow \quad \beta_{hkl}\cos\theta = \frac{K\lambda}{D} + 4\epsilon\sin\theta$$

where λ is the wavelength of the radiation (1.54056Å for Cu Kα radiation) and k is a constant equal to 0.91. In the above equation, the strain was assumed to be uniform in all crystallographic directions. The instrument-corrected broadening β_{hkl} corresponding to the diffraction peak was estimated using the relation:

$$\beta_{hkl} = \sqrt{(\beta)^2_{measured} + (\beta)^2_{instrumental}}$$

where $\beta_{measured}$ is the peak width measured at half-maximum intensity (FWHM) and $\beta_{instrumental}$ is the instrumental broadening which is 0.1 in the present case.

Table 1: Various parameters calculated from XRD patterns

Sample	[hkl]	2θ	d (Å)	Nelson-Riley Method			c (Å)	(c/a-1) ×100 (%)	W-H Method		Grain Size (μm)	ΔVf (%)	γ x10-14 (linesm-2)	Sf
				f (θ)	a cal (Å)	a corr (Å)			Crystallite Size (nm)	Strain (ε)				
BZT	[110]	31.29	2.8555	1.7490	4.0382	4.0421	4.0282	-0.343	63.10	-0.0488	14.23	1.617	2.59	0.05982
	[111]	38.58	2.3310	1.3716	4.0373									
	[200]	44.81	2.0203	1.1404	4.0407									
10BCT	[110]	31.37	2.8484	1.7440	4.0282	4.0340	4.0233	-0.267	63.38	-0.0417	17.46	1.584	2.49	0.05348
	[111]	38.65	2.3270	1.3686	4.0303									
	[200]	44.94	2.0148	1.1362	4.0296									
20BCT	[110]	31.46	2.8404	1.7383	4.0169	4.0264	3.9968	-0.733	68.99	-0.0331	17.83	1.455	2.10	0.04680
	[111]	38.79	2.3189	1.3627	4.0163									
	[200]	45.06	2.0097	1.1324	4.0194									
30BCT	[110]	31.48	2.8387	1.7371	4.0145	4.0175	4.0055	-0.298	72.21	-0.0316	20.03	1.390	1.92	0.04678
	[111]	38.83	2.3166	1.3610	4.0123									
	[200]	45.09	2.0084	1.1314	4.0169									
40BCT	[110]	31.52	2.8352	1.7346	4.0095	4.0028	4.0229	0.505	77.66	-0.0244	22.52	1.292	1.66	0.04675
	[111]	38.86	2.3149	1.3597	4.0094									
	[200]	45.21	2.0034	1.1276	4.0068									
50BCT	[110]	31.59	2.8290	1.7303	4.0008	3.9840	4.0344	1.265	81.77	-0.0158	25.64	1.227	1.50	0.03959
	[111]	38.97	2.3086	1.3551	3.9985									
	[200]	45.36	1.9971	1.1228	3.9942									
60BCT	[110]	31.63	2.8256	1.7278	3.9959	3.9767	4.0284	1.300	67.54	-0.0244	18.24	1.486	2.19	0.05949
	[111]	39.02	2.3058	1.3530	3.9936									
	[200]	45.42	1.9946	1.1209	3.9892									
70BCT	[110]	31.69	2.8203	1.7241	3.9885	3.9679	4.0285	1.529	55.46	-0.0331	14.19	1.811	3.25	0.05943
	[111]	39.08	2.3023	1.3505	3.9877									
	[200]	45.51	1.9909	1.1181	3.9818									
80BCT	[110]	31.79	2.8117	1.7179	3.9763	3.9575	4.0140	1.427	53.53	-0.0488	12.05	1.877	3.49	0.06530
	[111]	39.20	2.2956	1.3456	3.9759									
	[200]	45.66	1.9847	1.1134	3.9694									
90BCT	[110]	31.78	2.8126	1.7186	3.9775	3.9467	4.0307	2.129	50.09	-0.0489	11.65	2.006	3.99	0.07110
	[111]	39.22	2.2945	1.3447	3.9740									
	[200]	45.70	1.9830	1.1121	3.9661									
BCT	[110]	31.84	2.8074	1.7149	3.9702	3.9379	4.0590	3.075	41.41	-0.0574	9.55	2.429	5.83	0.07104
	[111]	39.29	2.2905	1.3418	3.9672									
	[200]	45.79	1.9794	1.1093	3.9587									

Fig. 3 shows a plot of $\beta \cos \theta$ versus $\sin \theta$ for the various reflecting planes. Extrapolation of the graph to $\sin \theta = 0$ gives $K\lambda/D$ as the intercept on the $\beta \cos \theta$ axis, from which the average D is deduced. The slope of the graph also gives the value of the average strain, ε, in the film. The values obtained are listed in **Table 1**. It has been observed that D increases with increasing x, reaches maximum at x=0.5 and then starts decreasing again. The initial increase in the crystallite size is attributed to the decreasing Zr^{4+} ions with increasing x. The lower values of crystallite size at lower x values (where Zr contents are more) are due to the slow diffusion of bigger Zr^{+4} ions replacing Ti^{+4} at B sites of oxygen octahedral, resulting in lower grain growth [13, 14]. Later on, the effect of increasing Ca contents starts dominating the effect of decreasing Zr from x=0.5 onwards to reverse the trend. It appears that the replacement of A^{2+} in ABO_3 perovskite structure with smaller Ca^{2+} tightens the structure which results in a significant decrease in the crystallite size with increasing Ca^{2+}[15].

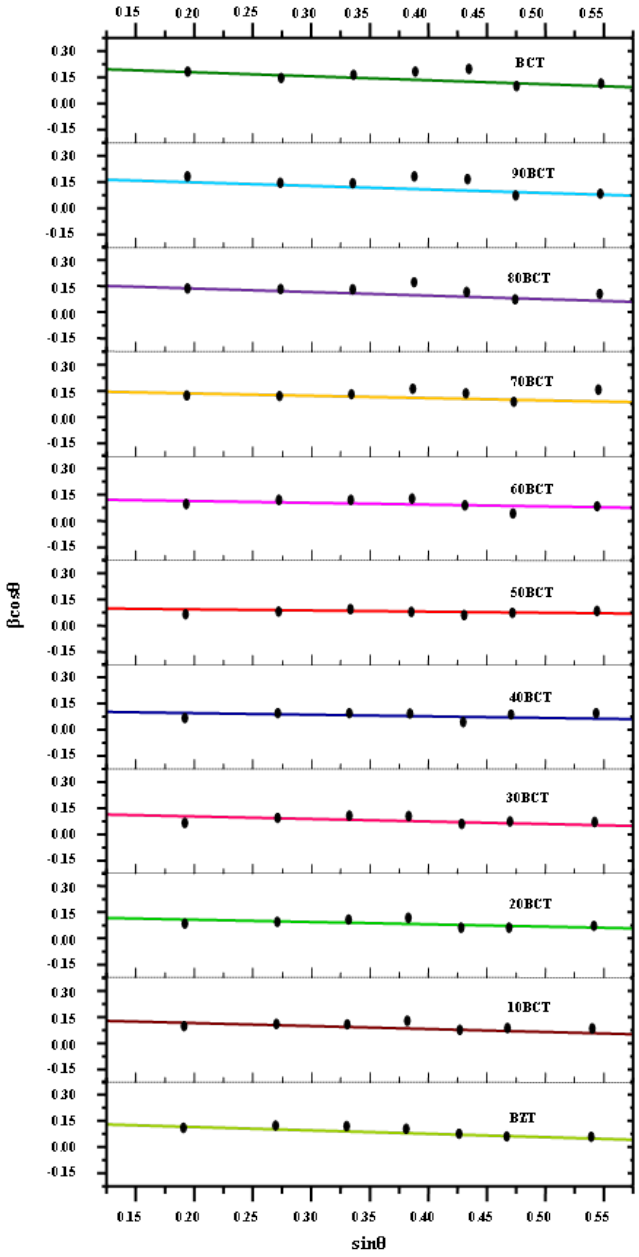

Fig. 3: Williamson-Hall Plot to calculate Crystallite Size and Lattice Strain.

Microstrain in the lattice is a measure of the distribution of lattice constants arising from crystal imperfections, such as lattice dislocations. Other sources of microstrain include the grain boundary triple junction, contact or sinter stresses, stacking faults and coherency stresses [12, 16]. The negative slopes of W-H Plots in **Figure3** suggest that there is presence of compressive strain in the ceramic samples which is minimum for the optimal composition x=0.5. The Zr^{4+} ions at B sites, due to their bigger size, exert pressure similar to hydrostatic pressure inside the oxygen octahedra, which leads to strained lattice. The stress inside the lattice decreases with the decreasing contents of Zr^{4+}. The value of strain reaches its minimum value at x=0.5 and then starts increasing till x=1 with increasing Ca^{2+} contents. The Ca^{2+} ions substituting Ba^{2+} tighten the lattice owing to their smaller radii and thus creating compressive stress in the ceramic. However, several groups [17, 18] suggested that there is a probability of Ca^{2+} occupying the Ti^{4+} site in $BaTiO_3$ lattice, provided the atomic concentration ratio of (Ba + Ca)/Ti is larger than unity. This ratio leads to excess barium and thus forcing Ca^{2+} to occupy the Ti^{4+} site. In addition, it is reported that the occupancy of Ca^{2+} in the Ti^{4+} site will create a compressive stress and lead to the distortion of the lattice [19]. In both the cases, Ca incorporation causes shrinkage of the lattice that further leads to compressive strain. Minimum lattice strain present in 50BCT enhances the mobility of the domains in the lattice.

The dislocation density (γ) was deduced from the expression [20]:

$$\gamma = \frac{c}{D^2}$$

where c is taken as unity at minimum dislocation density. The values of γ obtained are included in **Table 1**. Thus, dislocation density decreases with increasing crystallite size. It is pertinent to mention that stacking fault is one of the major layer defects in crystalline solids. The stacking fault probability (S_f) was computed using the following expression for [011] maximum intensity peak [20]:

$$s_f = \frac{2\pi^2\beta_{011}}{45(3tan\theta_{011})^{1/2}}$$

where $\beta_{011}$is the Corrected FWHM corresponding to Bragg's angle θ_{011} for maximum intensity (011) peak. The values of $S_f$obtained using above equation are also listed in **Table 1,** and from there, we can infer that 50BCT has the lowest probability of stacking fault defects which gradually increases we move away from 50BCT on either side. The stacking fault is found to be maximum for BCT ceramic which accounts for its high compressive strain.

In order to estimate the densityof grain boundaries, the excess free volume associated with the grain boundaries was calculated using the following expression [21]:

$$\Delta V_F = \frac{(L + d/2)^2 - L^2}{L^2}$$

where L is the crystallite size and d is the mean width of the grain boundaries. In most of the prior calculation of the excess free volume, the width of the grain boundary has been assumed to be constant (d = 1nm), independent of the grain size. It was observed that the grain boundary free volume increases with decrease in crystallite size (**Table 1**). Also, with the decrease in grain size, the number of grain boundaries per unit area and the number of boundary interfaces increase.

Fig. 4 illustrates the surface micrograph of all compositions. The surface morphology appeared to be changing with changing x-value. The grain size calculated by linear intercept method for different compositions (tabulated in **Table 1**), was found to decline gradually on either side of optimal composition at x=0.5 where it reaches maximum. The trend of

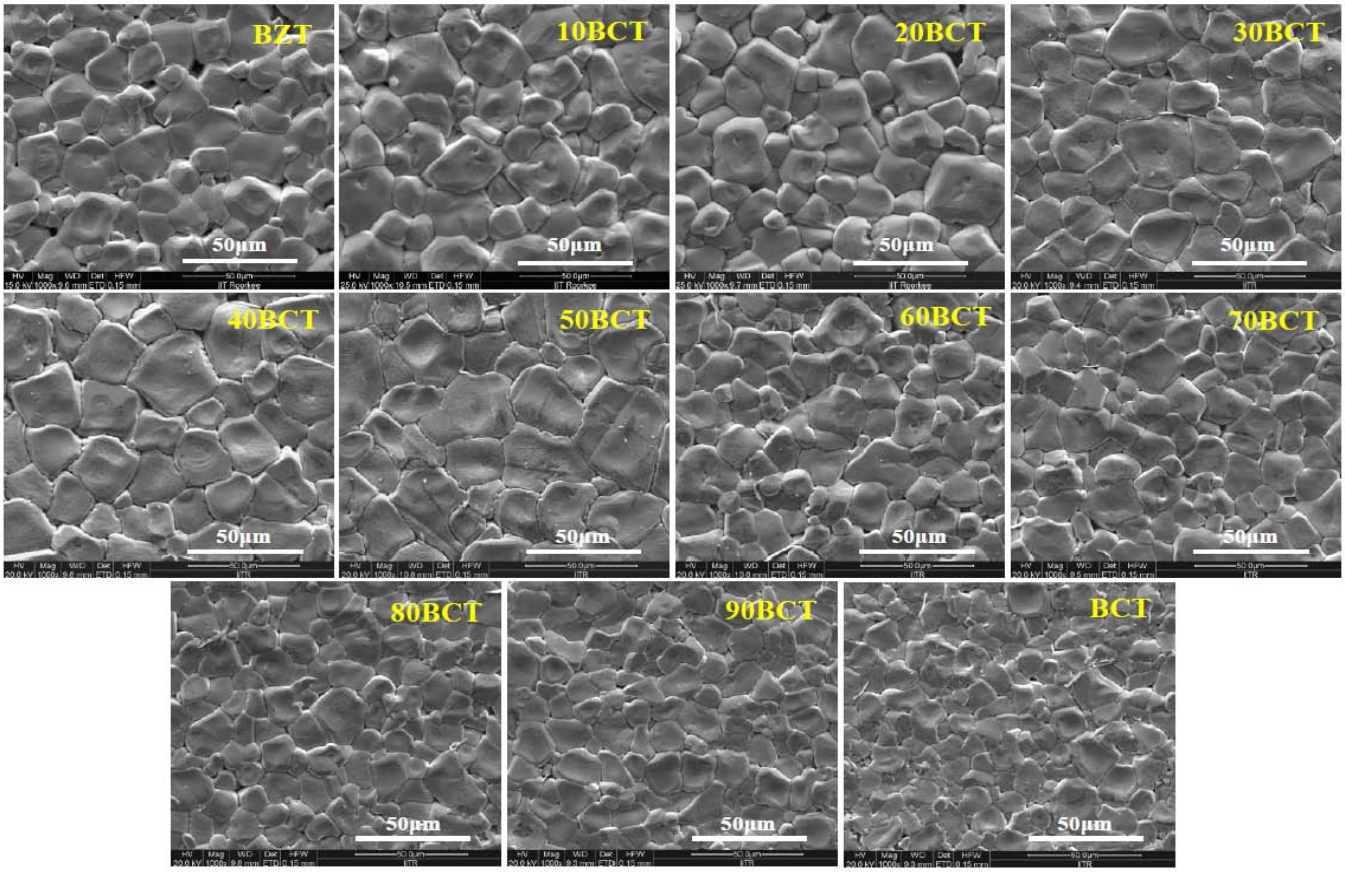

Fig. 4: FESEM micrographs of BZT-*x*BCT.

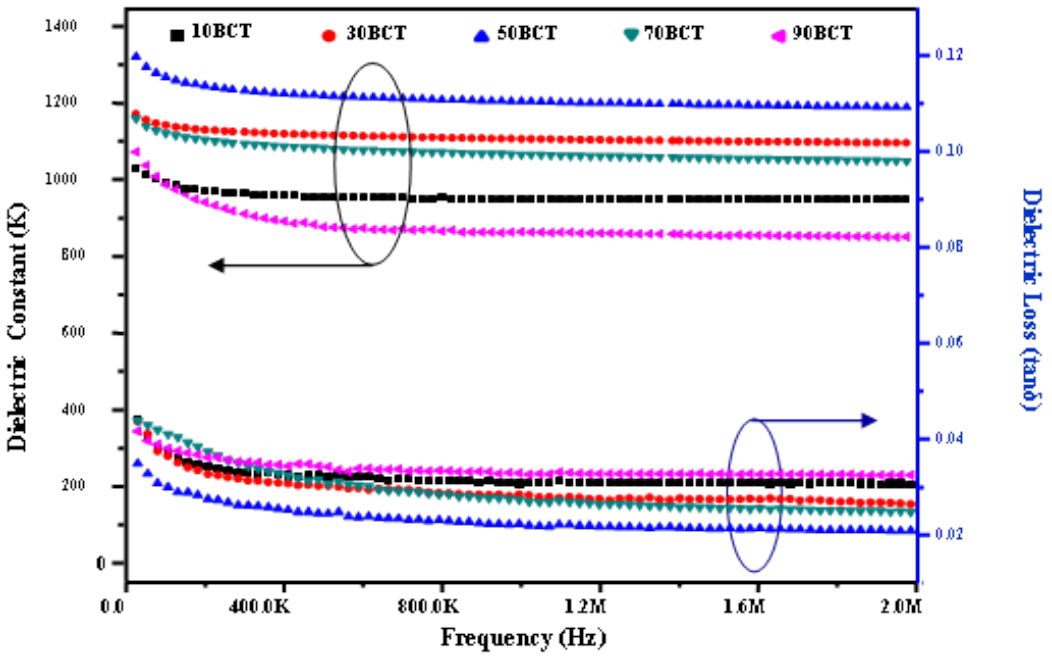

Fig. 5: The dielectric constant (ϵ) and dielectric loss (tan δ) as function of frequency

changing grain size found in FESEM analysis supports the trend of changing crystallite size as given by XRD analysis. It was observed that the grain sizes, determined by FESEM are much bigger than that crystallite size calculated by XRD. This difference is ascribed to the fact that FESEM shows agglomeration of the particles whereas XRD gives an average crystallite size. The XRD and FESEM data can be reconciled by the fact that smaller primary particles have a large surface free energy and would, therefore, tend to agglomerate faster and grow into larger grains. We can clearly see that there is a loss of densification, both at higher and lower *x*-value due to the non-uniform grain growth and reasons for which have already been explained in previous paragraphs [22].

The dielectric constant(ϵ)and dielectric loss δ)(tan measured as a function of frequency at room temperature by applying small ac signal of 500 mV amplitude. **Figure5** shows the frequency dispersion of the dielectric constant and dielectric loss of BZT-*x*BCT ceramics in the range from 1KHz to 2 MHz. The dielectric constant shows same tendency and decreases with increasing frequency, which is a general behavior of normal dielectric/ferroelectric materials. The delay in the response towards the impressed alternating electric field at high frequencies leads to loss and hence decline in dielectric constant [23]. The composite with larger grain size has higher dielectric constant and lower loss. The dielectric constant is maximum for 50BCT and declines on either side of this composition as grain size decreases. The lower values of dielectric constant for other compositions may be attributed to the increasing number of grain boundaries with decreasing grain size. The large number of grain boundaries leads to the lower polarization intensity and therefore contribute to the lower dielectric constant [24].

4. CONCLUSION

XRD analysis revealed that crystallite size and peak intensity are maximum for 50BCT composite ceramic. It also established that 50BCT shows minimum strain, minimum dislocation density, minimum stacking fault probability and minimum excess free volume among all the compositions, which facilitate domain switching to some extent. FESEM analysis confirmed the large and uniform grain growth of ceramic at x=0.5 which is held responsible for its enhanced dielecric properties. The grain size effect supplements morphotropic phase boundary mechanism to make 50 BCT a superior electroceramic. By varying Zr/Ti and Ba/Ca ratios of the solid solution, the dielectric constant can be tailored to suitable values for designing tunable capacitor and Multilayer Ceramic Capacitor.

REFERENCES

[1] W. Liu, X. Ren, Phys. Rev. Lett. 103 (2009) 257602.

[2] S. J. Kuang, X. G. Tang, L.Y. Li, Y. P. Jiang, Q. X. Liu, Scr. Mater. 61 (2009) 68.

[3] C. Bhardwaj, D. KaurCurr. Appl. Phys. 12 (5) (2012) 1239.

[4] Wei. Li, R. Chu, P. Fu, G. Zang, Mater. Lett. 64 (2010) 2325.

[5] B. D. Cullity, Elements of X-ray Diffraction. Addison-Wesley Publishing Company Inc., California, 1956.

[6] J.B. Nelson, D.P. Riley, Proc. Phys. Soc. London 57 (1945) 160.

[7] F. Moura, J. All. Com. 462 (2008) 129.

[8] N. Nanakorn, P. Jalupoom, N. Vaneesorn, A. Thanaboonsombut, Ceram. Int. 34 (2008) 779.

[9] M. R. Panigrahi, S. Panigrahi, Physica B 405 (2010) 1787.

[10] L. N. Gao, J. W. Zhai, X. Yao, J. Sol-Gel Sci. Technol. (2008) 45.

[11] C. Suranarayana, M.G. Norton, X-ray Diffraction: A Practical Approach NewYork (1998).

[12] A. K. Zak, W. H. Abd, M. E. Abrishami, R. Yousefi, Solid State Sci. 13 (2011) 251.

[13] Y. Zhi, R. Guo, A. S. Bhalla, J. Appl. Phys. 88 (2000) 410.

[14] Y. Zhi, R. Guo, A. S. Bhalla, J. Cryst. Growth 223 (2001) 460.

[15] P. Victor, R. Ranjith, S. B. Karupanidhi, J. Appl. Phys. 94 (2003) 7702.

[16] J. Zhang, Y. Zhang, K.W. Xu, V. Ji, Solid State Commun. 139 (2006) 87.

[17] Y. H. Han, J. B. Appleby, D. M. Smyth, J. Am. Ceram. Soc. 70 (1987) 96.

[18] X.W. Zhang, Y.H. Han, M. Lal, D.M. Smyth, J. Am. Ceram. Soc. 70 (1987) 100.

[19] Z.Q. Zhuang, M.P. Harmer, D.M. Smyth, R.E. Newnham, MRS Bull. 22 (1987) 1329.

[20] F. C. Eze, Mater. Chem. Phys. 89 (2005) 205.

[21] A. Kumar, D. Singh, D. Kaur, Surf. Coat. Technol. 203 (2009) 1596.

[22] X. Wang, H. Yamada, C. N. Xua, Appl. Phys. Lett. 86 (2005) 022905.

[23] C. Bhardwaj, B.S.S. Daniel, D. KaurJ. Phys. Chem. Solids 74 (1) (2013) 94.

[24] F. Yan, P. Bao, H. L. W. Chan, C. L. Choy, Y. Wang, Thin Solid Films 406 (2002) 282.